

Dependence of electric field domain relocation dynamics on contact conductivity in semiconductor superlattices

Huidong Xu and Stephen W. Teitworth

Department of Physics, Duke University, Box 90305, Durham, North Carolina 27708-0305, USA

(Received 1 July 2007; published 3 December 2007)

Numerical simulation results are presented for a discrete drift-diffusion rate equation model that describes electronic transport due to sequential tunneling between adjacent quantum wells in weakly coupled semiconductor superlattices. We study the dependence on contact conductivity σ of current-voltage characteristics and transient current response to abrupt steps in applied voltage. For intermediate values of σ , three qualitatively distinct transient responses—each associated with a different mechanism for the *relocation* of a static charge accumulation layer—are observed for different values of voltage step V_{step} ; these involve, respectively, (1) the motion of a single charge accumulation layer, (2) the motion of an injected charge dipole, and (3) the motion of an injected monopole. A critical value of σ is identified above which the injected dipole mechanism is not observed for any value of V_{step} . Furthermore, at very low σ , we find a reversed static field configuration, i.e., with the high-field domain adjacent to the emitter contact.

DOI: [10.1103/PhysRevB.76.235302](https://doi.org/10.1103/PhysRevB.76.235302)

PACS number(s): 73.63.-b, 73.50.Fq

I. INTRODUCTION

Since the pioneering work of Esaki and Chang,¹ semiconductor superlattices have been the focus of intense study for their unique electronic transport and optical properties. Following the experimental observation of current branches in doped, weakly coupled superlattices by Choi *et al.*² in 1988 and the subsequent attribution of these branches to static electric field domain formation, there has been a great deal of research on electric field domain phenomena in GaAs/AlAs superlattices.³⁻⁵ Furthermore, related static field domain formation effects have recently been reported for multiple quantum well devices such as quantum cascade laser structures⁶ and quantum well infrared photodetectors.⁷

One important consequence of the presence of static field domains in GaAs/AlAs superlattices (SLs) is to yield nontrivial and unexpected transient behavior in the current response to abrupt changes in applied voltage. Recent transient experiments of Luo *et al.*⁸ and Rogozia *et al.*⁹⁻¹¹ have reported both stochastic and complex deterministic aspects of current switching behavior and have demonstrated the potential of such measurements to elucidate the underlying relocation dynamics of the domain boundaries—which correspond to charge depletion or accumulation layers—from one quantum well of the SL to another. These initial experiments have been accurately described in terms of a spatially discrete, drift-diffusion transport model which treats the electronic transport in the weakly coupled SL using a system of coupled ordinary differential equations based on microscopic tunneling Hamiltonians.¹²⁻¹⁸ Specifically, Amann *et al.*¹⁴ first reported a domain relocation scenario which proceeds via an *injected charge dipole* and has a relatively long overall time to complete; this relocation scenario was subsequently verified in transient experiments by Rogozia *et al.*¹⁰ and is also referred to as a “tripole-dipole” since it typically involves the simultaneous motion of three localized charge layers through the SL. Additionally, Amann *et al.*¹⁴ reported a relatively fast relocation scenario mediated by an *injected charge monopole*

for a somewhat larger contact conductivity value, but this has not yet been observed experimentally. In more recent work, Bonilla *et al.* studied the effect of different voltage ramping times on the relocation scenario and observed that the ends of the individual current branches have small, stable oscillations, resulting from a Hopf bifurcation so that the stationary current state becomes unstable.¹³ In both of these papers, the simulation results focused on a small set of values for contact conductivity σ , mostly selected to approximate the σ value for experimental samples of Rogozia *et al.*¹⁰

In this paper, we study the dependence of time-averaged current-voltage (I - V) characteristics and domain relocation dynamics on contact conductivity σ while keeping the doping profile within the SL fixed. This is particularly significant because σ is straightforward to vary in experimental structures, for example, by varying the doping level in the contact layers or the thickness of the first barrier of the SL. For larger σ values that correspond to the presence of static domains, we find that the switching dynamics is strongly dependent on the σ value while the static I - V curves change only slightly. Principal results include that the injected charge dipole relocation mechanism and the small-amplitude current oscillations are suppressed for σ values modestly larger than those previously studied. At the same time, we find that a relatively fast injected charge monopole relocation mechanism becomes predominant for these larger σ values. The transition between these two behaviors occurs for a narrow range of σ values that are close to the σ value for which the contact current-field (J - F) characteristic passes through the first local maximum in superlattice J - F characteristic. This transition is reminiscent of that reported in studies of the effect of contact conductivity on current oscillations and space charge waves in the bulk Gunn effect.¹⁹ In that case, it was found that for smaller σ values, current oscillations correspond to recycling charge dipole waves, while for larger σ values, relatively fast monopole waves predominate. In both cases, the creation of a dipole requires a region of depleted

electron charge near the contact.

For smaller values of σ , we find that static domains and associated time-independent current branches give way to moving space charge waves and associated time-periodic current oscillations, such that the time-averaged I - V curves are relatively smooth. This transition from static to time-dependent behavior is analogous to that which occurs as the SL doping level is reduced while the σ value is held fixed.^{20,21} Finally, we have identified a reversed static electric field configuration in simulations for very *low* values of σ in which the high-field domain forms next to the emitter contact, with the low-field domain next to the collector; these two regions are separated by a relatively wide static charge depletion layer.

The remaining sections of the paper are organized as follows. In Sec. II, the Kubo formula is applied to a microscopic tunneling Hamiltonian appropriate for weakly coupled superlattices in order to derive a discrete, drift-diffusion rate equation model that is equivalent to one recently used by Bonilla *et al.*¹³ Section III describes the non-dimensionalization of the rate equation model and presents a form of the model that is well suited to numerical simulation. In Sec. IV, we discuss the dependence of time-averaged I - V curves on contact conductivity σ , as well as the reversed static field configuration for very small σ values. Section V describes the principal domain relocation scenarios that occur in response to abrupt changes in applied voltage and maps out how these depend on σ and voltage step size V_{step} . Finally, the main results of the paper are summarized in Sec. VI.

II. TUNNELING HAMILTONIAN AND DISCRETE RATE EQUATION MODEL

The discrete rate equation model that we employ for the simulations below has been developed over the past several years and has proven useful to model experimental results with good accuracy for parameters so far studied (for a review, see Ref. 17). A heuristic derivation of the model using Fermi's golden rule has also been presented in Ref. 17. Here, we present an alternative derivation of the discrete rate equation model starting from a microscopic tunneling Hamiltonian that aptly characterizes the weakly coupled superlattice. Among the advantages of this approach are that it is relatively straightforward to generalize to include additional physical effects, such as phonon scattering, phonon- or photon-assisted tunneling, or electron-electron interaction.¹⁶ Additionally, this approach makes clear that the derived rate equation model is the result of a consistent first-order perturbation theory; such an approach could also serve as a starting point for calculations that are higher order in tunnel coupling as would be needed, e.g., if one were to consider somewhat thinner barriers.

The tunneling Hamiltonian is written as follows:^{22,23}

$$\begin{aligned} H_{total} &= H + H_T \\ &= \sum_{i=0}^{N+1} H_i + \sum_{j=0}^N H_{T_j} \end{aligned} \quad (1a)$$

$$\begin{aligned} &= \sum_{i=0}^{N+1} \sum_{\mathbf{k}_i} E_{i\mathbf{k}_i} c_{i\mathbf{k}_i}^\dagger c_{i\mathbf{k}_i} + \sum_{j=0}^N \sum_{\mathbf{k}_j, \mathbf{k}_{j+1}} (T_{\mathbf{k}_{j+1}\mathbf{k}_j} c_{j+1\mathbf{k}_{j+1}}^\dagger c_{j\mathbf{k}_j} + \text{H.c.}). \end{aligned} \quad (1b)$$

Here, the summation over i extends over the left lead ($i=0$), the quantum wells ($i=1-N$), and the right lead ($i=N+1$). The operators $c_{i\mathbf{k}_i}^\dagger$ ($c_{i\mathbf{k}_i}$) denote creation (annihilation) operators for electrons in the i th well or lead with three-dimensional momentum \mathbf{k}_i and satisfy standard fermionic commutation rules: $\{c_{i\mathbf{k}_i}, c_{j\mathbf{k}_j}\} = c_{i\mathbf{k}_i} c_{j\mathbf{k}_j} + c_{j\mathbf{k}_j} c_{i\mathbf{k}_i} = 0$, $\{c_{i\mathbf{k}_i}^\dagger, c_{j\mathbf{k}_j}^\dagger\} = 0$, and $\{c_{i\mathbf{k}_i}, c_{j\mathbf{k}_j}^\dagger\} = \delta_{ij} \delta_{\mathbf{k}_i, \mathbf{k}_j}$. The amplitude $T_{\mathbf{k}_{j+1}\mathbf{k}_j}$ denotes the tunneling matrix element between the j th and $(j+1)$ th well and/or lead. In this model, the unperturbed Hamiltonian H denotes a sum of individual Hamiltonians for each quantum well or lead and assumes that they are uncoupled from one another. The unperturbed single-electron states have absolute energies denoted by $E_{i\mathbf{k}_i}$ which are defined such that, for all i , the zero of energy is taken as the conduction band edge in the left lead (i.e., the emitter contact). Below, it will be convenient to define an alternative quantity $\epsilon_{\mathbf{k}_i}$ as the energy of the single-particle states relative to the conduction band edge of the i th well and/or lead. The relationship between these two ways of expressing energy is summarized in $E_{i\mathbf{k}_i} = \epsilon_{\mathbf{k}_i} + eV_i$, where $e < 0$ is the electron charge and V_i denotes the electric potential at the position of the i th well and/or lead. Furthermore, each quantum well comprises a set of two-dimensional free electron gases—one for each subband. Each quantum well or lead is assumed to be characterized by a distinct *internal* chemical potential value μ_i , and these are determined below using a self-consistency argument based on the classical Poisson's equation. The entire system is assumed to have temperature T . The second term in Eq. (1b), H_T , represents the effect of tunnel coupling between adjacent wells and/or leads and is treated as a small perturbation, expected to be appropriate for weakly coupled superlattices. It should also be noted that when an energetic electron tunnels into a quantum well, it is assumed to relax instantly to the ground state for that quantum well.

The tunneling current from the i th period to $(i+1)$ th period in steady state may be expressed in terms of the rate of change of the number of particles in the i th period.²⁴ This rate can be expressed in terms of a commutator of the number operator $N_i = \sum_{\mathbf{k}_i} c_{i\mathbf{k}_i}^\dagger c_{i\mathbf{k}_i}$ with the total Hamiltonian:

$$\begin{aligned} e\dot{N}_i &= \frac{i}{\hbar} [H_{total}, eN_i] \\ &= \frac{i}{\hbar} [H_{T_{i-1}}, eN_i] + \frac{i}{\hbar} [H_{T_i}, eN_i] \\ &= \hat{I}_{i-1 \rightarrow i} - \hat{I}_{i \rightarrow i+1}. \end{aligned} \quad (2)$$

Here, $\hat{I}_{i-1 \rightarrow i} = \frac{i}{\hbar} [H_{T_{i-1}}, eN_i]$ corresponds to the tunneling cur-

rent operator from $(i-1)$ th period to i th period and a similar definition applies for $\hat{I}_{i \rightarrow i+1}$. Going to the interaction representation, the operators transform according to $H_T(t') = e^{iHt'} H_T e^{-iHt'}$ and $\hat{I}_{i \rightarrow i+1}(t) = e^{iHt} \hat{I}_{i \rightarrow i+1} e^{-iHt}$, and we may express the tunneling current from i th period to $(i+1)$ th period in terms of the following Kubo formula:^{24,25}

$$I_{i \rightarrow i+1}(t) = \int_{-\infty}^t dt' \langle [\hat{I}_{i \rightarrow i+1}(t), H_T(t')] \rangle. \quad (3)$$

Here, it is understood that the expectation value is computed using the appropriate unperturbed thermodynamic ground states for the two electron gases in the i th and $(i+1)$ th wells. Note that this expression is first order in the perturbation, H_T .

The evaluation of Eq. (3) is straightforward if somewhat lengthy, and the resulting current can be simply expressed as²⁵

$$I_{i \rightarrow i+1} = \frac{4\pi e}{\hbar} \sum_{\mathbf{k}_i, \mathbf{k}_{i+1}} |T_{\mathbf{k}_{i+1}, \mathbf{k}_i}|^2 \delta(\epsilon_{\mathbf{k}_{i+1}} - \epsilon_{\mathbf{k}_i} - eF_i l) [n_F(\epsilon_{\mathbf{k}_{i+1}} - \mu_{i+1}) - n_F(\epsilon_{\mathbf{k}_i} - \mu_i)], \quad (4)$$

where $n_F(x) = [1 + \exp(x/k_B T)]^{-1}$ denotes the Fermi function, and we have defined F_i as the average electric field between wells i and $i+1$ so that, in terms of electric potential, one writes $-F_i = (V_{i+1} - V_i)/l$. The tunneling matrix element is calculated using a method due to Bardeen.^{23,25,26}

$$|T_{\mathbf{k}_{i+1}, \mathbf{k}_i}|^2 = \frac{\hbar^4}{4m^{*2}} \mathcal{T}_i(\epsilon_{i,z}) \delta_{\mathbf{k}_{i\perp}, \mathbf{k}_{i+1\perp}}, \quad (5)$$

where

$$\mathcal{T}_i(\epsilon_{i,z}) = \frac{16k_i^2 k_{i+1}^2 \alpha_i^2 (k_i^2 + \alpha_i^2)^{-1} (k_{i+1}^2 + \alpha_i^2)^{-1}}{(w + \alpha_{i-1}^{-1} + \alpha_i^{-1})(w + \alpha_{i+1}^{-1} + \alpha_i^{-1}) e^{2\alpha_i d}}, \quad (6)$$

$$\hbar k_i = \sqrt{2m^* \epsilon_{i,z}}, \quad (7)$$

$$\hbar k_{i+1} = \sqrt{2m^* [\epsilon_{i,z} + e(d+w)F_i]}, \quad (8)$$

$$\hbar \alpha_{i-1} = \sqrt{2m^* \left[|e|V_b + e \left(d + \frac{w}{2} \right) F_i - \epsilon_{i,z} \right]}, \quad (9)$$

$$\hbar \alpha_i = \sqrt{2m^* \left[|e|V_b - \frac{ewF_i}{2} - \epsilon_{i,z} \right]}, \quad (10)$$

$$\hbar \alpha_{i+1} = \sqrt{2m^* \left[|e|V_b - e \left(d + \frac{3w}{2} \right) F_i - \epsilon_{i,z} \right]}. \quad (11)$$

Here, $\mathbf{k}_{i\perp}$ is the component of \mathbf{k}_i perpendicular to the current flow, $\epsilon_{i,z}$ is the energy in the parallel direction, i.e., the z component of the total energy $\epsilon_{\mathbf{k}_i}$, d denotes the width of one

barrier, w the width of one well, and m^* the electron effective mass (taken as 8.43×10^{-32} kg corresponding to an appropriately weighted average of GaAs and AlAs effective masses). Additionally, $|e|V_b$ is the barrier height in the absence of an applied potential drop (taken as 0.982 eV for the GaAs/AlAs interface).

In order to calculate the current $I_{i \rightarrow i+1}$, we carry out the summation in Eq. (4) in the parallel directions and sum over the subband energy levels by inserting a spectral function $A_\nu(\epsilon_z)$, which is centered at ν th level \mathcal{E}_ν with a scattering width γ_ν ,

$$A_\nu(\epsilon_z) = \frac{\gamma_\nu / \pi}{(\epsilon_z - \mathcal{E}_\nu)^2 + \gamma_\nu^2}. \quad (12)$$

For transport between adjacent quantum wells, Eq. (4) can be written as

$$I_{i \rightarrow i+1} = \frac{\pi \hbar^3 e}{m^{*2}} \sum_{\nu=1}^{n_{\max}} \sum_{\mathbf{k}_{i\perp}, \mathbf{k}_{i+1\perp}} \int A_1(\epsilon_{i,z}) d\epsilon_{i,z} \int A_\nu(\epsilon_{i+1,z}) d\epsilon_{i+1,z} \times \mathcal{T}_i(\epsilon_{i,z}) \delta(\epsilon_{\mathbf{k}_{i+1}} - \epsilon_{\mathbf{k}_i} - eF_i l) \times [n_F(\epsilon_{\mathbf{k}_{i+1}} - \mu_{i+1}) - n_F(\epsilon_{\mathbf{k}_i} - \mu_i)] \delta_{\mathbf{k}_{i\perp}, \mathbf{k}_{i+1\perp}}. \quad (13)$$

Carrying out the \mathbf{k}_\perp summations and the integration over $\epsilon_{i+1,z}$, dividing by cross-sectional area, and replacing the remaining integration variable $\epsilon_{i,z}$ with ϵ , we can write the current density as

$$J_{i \rightarrow i+1} = e \frac{\hbar k_B T}{2m^*} \sum_{\nu=1}^{n_{\max}} \int_0^{+\infty} A_1(\epsilon) A_\nu(\epsilon + eF_i l) \times \mathcal{T}_i(\epsilon) \ln \left(\frac{1 + e^{(\mu_i - \epsilon)/k_B T}}{1 + e^{(\mu_{i+1} - \epsilon)/k_B T}} \right) d\epsilon, \quad (14)$$

which is identical to the tunneling current expression derived using a Fermi's golden rule approach as described, e.g., in Ref. 17.

The integral of Eq. (14) can be approximately calculated by assuming that the scattering width is small compared to the subband energies and chemical potentials:

$$J_{i \rightarrow i+1} = \frac{ev^f(F_i)}{l} \left(n_i - \frac{m^* k_B T}{\pi \hbar^2} \ln \left[1 + \exp \left(-\frac{eF_i l}{k_B T} \right) \right] \times \left[\exp \left(\frac{\pi \hbar^2 n_{i+1}}{m^* k_B T} \right) - 1 \right] \right), \quad (15)$$

where we have defined the two-dimensional electron density in the i th well,

$$n_i = \frac{m^* k_B T}{\pi \hbar^2} \ln [1 + e^{(\mu_i - \mathcal{E}_1)/k_B T}], \quad (16)$$

and the effective electron drift velocity,

$$v^{(f)}(F_i) = \sum_{j=1}^{n_{\max}} \frac{\hbar^3 l (\gamma_1 + \gamma_j) \mathcal{T}_i(\mathcal{E}_1)}{2m^{*2} (\mathcal{E}_1 - \mathcal{E}_j + eF_i l)^2 + (\gamma_1 + \gamma_j)^2}. \quad (17)$$

Equation (15) above indicates that, in general, the tunneling current density depends on the variables n_i , n_{i+1} , and F_i ,

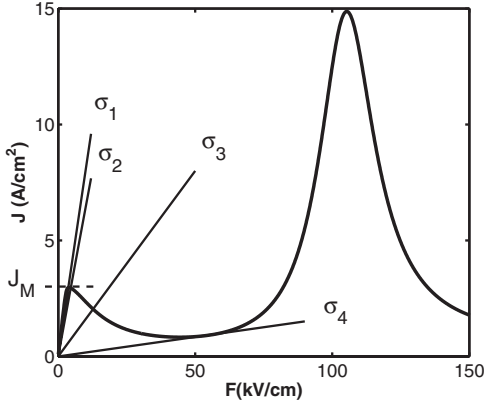


FIG. 1. Tunneling current density for well-to-well transport vs electric field under uniform electric field conditions $J_{SL}(F)$. The straight lines represent Ohmic contact characteristics for different σ values: $\sigma_1=0.08$ ($\Omega \text{ m}$) $^{-1}$, $\sigma_2=0.064$ ($\Omega \text{ m}$) $^{-1}$, $\sigma_3=0.016$ ($\Omega \text{ m}$) $^{-1}$, and $\sigma_4=0.00168$ ($\Omega \text{ m}$) $^{-1}$.

and this dependence can be clarified by writing $J_{i \rightarrow i+1}(n_i, n_{i+1}, F_i)$. In Fig. 1, we plot the field dependence under the condition of uniform electric field (equivalently, no net space charge) so that $n_i = n_{i+1} = N_D$, where N_D is the two-dimensional doping density in the i th well; this defines the SL current-field characteristic which we denote as follows: $J_{SL}(F_i) \equiv J_{i \rightarrow i+1}(N_D, N_D, F_i)$.

The fundamental tunneling current expression, Eq. (4), can also be used to develop (generally nonlinear) current-field characteristics that describe transport from the emitter to the first quantum well or from the last well into the collector. A key ingredient is the structure of electronic states in the emitter and/or collector, typically different than the structure of states in the quantum wells. One plausible approach treats the emitter as a three-dimensional Fermi gas of electrons with local chemical potential determined by the donor concentration in the contact region.^{18,22} We have performed our calculations using both this microscopic boundary condition and an Ohmic boundary condition and we find good agreement, provided that the effective σ value is chosen so that the microscopically based contact J - F characteristic and the Ohmic characteristic both intersect the J - F curve of the SL at the same point (cf. Fig. 1). A separate question of importance for experiment is to relate the effective value of σ to parameters that can be controlled in real superlattices, for example, the donor concentrations in the emitter and collector and the thicknesses of the first and last SL barriers. The connection between σ and the emitter donor concentration is discussed in the Appendix. For the present study, we use the following Ohmic boundary conditions:^{14,18}

$$J_{0 \rightarrow 1} = \sigma F_0, \quad (18)$$

$$J_{N \rightarrow N+1} = \sigma F_N \frac{n_N}{N_D}, \quad (19)$$

where σ denotes the effective contact conductivity.

Integrating over one SL period, the Poisson's equation and the charge continuity equation are expressed as

$$F_i - F_{i-1} = \frac{e}{\epsilon}(n_i - N_D), \quad i = 1, \dots, N, \quad (20)$$

$$\epsilon \frac{dn_i}{dt} = J_{i-1 \rightarrow i} - J_{i \rightarrow i+1}, \quad i = 1, \dots, N, \quad (21)$$

where ϵ is the dielectric constant. Equations (20) and (21) together with the boundary conditions, Eqs. (18) and (19), comprise the sequential tunneling model that we simulate, which takes the form of a rate equation model with the nonlinear drift-diffusion current of Eq. (15). The fundamental dynamical variables are the averaged field values in each quantum well plus the field values in the injecting and receiving contacts. Differentiating Eq. (20) with respect to time gives

$$\epsilon \frac{dF_i}{dt} + J_{i \rightarrow i+1} = J(t), \quad i = 0, \dots, N, \quad (22)$$

in which the total current density $J(t)$ is the same for all periods. The bias condition is

$$\frac{1}{N+1} \sum_{i=0}^N F_i = \frac{V(t)}{(N+1)l}, \quad (23)$$

where $V(t)$ is the total voltage bias across the sample.

For simulations reported below, the parameter values generally follow the experimental structure of Rogozia *et al.*¹⁰ Thus, the number of SL periods is $N=40$ while the doping density in each quantum well is $N_D=1.5 \times 10^{11} \text{ cm}^{-2}$. The widths of each quantum well and barrier are 9 and 4 nm, respectively, which implies that the subband energies are $\mathcal{E}_1=44 \text{ meV}$, $\mathcal{E}_2=180 \text{ meV}$, and $\mathcal{E}_3=410 \text{ meV}$. Additionally, we assume that the scattering widths are independent of subband index so that $\gamma = \gamma_j = 8 \text{ meV}$.^{13,14}

III. NUMERICAL APPROACH

To numerically solve the system, we adopt the approach of Bonilla *et al.*¹³ First, we convert the equations to dimensionless form by introducing the following dimensionless quantities:

$$\begin{aligned} E_i &= \frac{F_i}{F_M}, \quad \tilde{n}_i = \frac{n_i}{N_D}, \quad \tilde{J}_{i \rightarrow i+1} = \frac{J_{i \rightarrow i+1}}{J_M}, \\ \tilde{t} = \frac{t}{t_0} &\equiv \frac{J_M t}{\epsilon F_M}, \quad v(E_i) = \frac{v^{(f)}(F_i)}{v_M}, \quad \phi = \frac{V}{V_0} \equiv \frac{V}{(N+1)F_M l}, \\ \tilde{\sigma} = \frac{\sigma}{\sigma_c} &\equiv \frac{F_M \sigma}{J_M}, \quad v_M = \frac{J_M l}{e N_D}, \quad x_0 = \frac{\epsilon F_M l}{e N_D}. \end{aligned} \quad (24)$$

The characteristic scale values that are appropriate for a temperature of $T=5 \text{ K}$ and the parameters of the superlattice sample we are simulating are shown in Table I.

The values F_M and J_M denote the coordinates of the first peak of the tunneling current $J_{i \rightarrow i+1}$ of Eq. (15) under uniform field conditions so that $n_i = n_{i+1} = N_D$, cf. Fig. 1. The scale for contact conductivity is defined by σ_c which corre-

TABLE I. Typical scales for the 9 nm/4 nm GaAs/AlAs SL at $T=5$ K (Ref. 13).

F_M (kV/cm)	J_M (A/cm ²)	v_M (m/s)	x_0 (nm)	t_0 (ns)	σ_c (Ω m) ⁻¹	V_0 (V)
3.945	3.127	1.691	2.494	2.066	0.07924	0.205

sponds to the slope of a straight line that passes through the local maximum in the J - F curve of Fig. 1. It should be noted that the experimental sample of Ref. 10 had an estimated $\sigma_{exp} \approx 0.0397$ (Ω m)⁻¹, and previous simulations of transient response have focused on this value, about half that of σ_c . With the above definitions, the model equations Eqs. (15), (18)–(20), (22), and (23), can be written in dimensionless form, respectively, as

$$\frac{dE_i}{d\tilde{t}} + \tilde{J}_{i \rightarrow i+1} = \tilde{J}, \quad i = 0, \dots, N, \quad (25)$$

$$\tilde{n}_i = \frac{E_i - E_{i-1}}{\nu} + 1, \quad i = 1, \dots, N, \quad (26)$$

$$\sum_{i=0}^N E_i = (N+1)\phi(t), \quad (27)$$

$$\tilde{J}_{i \rightarrow i+1} = v(E_i) \{ \tilde{n}_i - \rho_0 \ln[1 + e^{-aE_i}(e^{\tilde{n}_{i+1}/\rho_0} - 1)] \}, \quad i = 1, \dots, N-1, \quad (28)$$

$$\tilde{J}_{0 \rightarrow 1} = \tilde{\sigma} E_0, \quad (29)$$

and

$$\tilde{J}_{N \rightarrow N+1} = \tilde{\sigma} E_N \tilde{n}_N, \quad (30)$$

where we have defined the following dimensionless parameters:

$$\nu = \frac{eN_D}{\epsilon F_M} \approx 5.212, \quad \rho_0 = \frac{m^* k_B T}{\pi \hbar^2 N_D}, \quad a = \frac{e l F_M}{k_B T}. \quad (31)$$

Summing Eq. (26) from $i=0$ to N , we find that

$$\tilde{J} = \frac{d\phi(t)}{d\tilde{t}} + \frac{1}{N+1} \sum_{i=0}^N \tilde{J}_{i \rightarrow i+1}. \quad (32)$$

Inserting this result back into Eq. (25), we obtain an equivalent equation which is used in our simulations,

$$\frac{dE_i}{d\tilde{t}} = \frac{d\phi(t)}{d\tilde{t}} + \frac{1}{N+1} \sum_{j=0}^N \tilde{J}_{j \rightarrow j+1} - \tilde{J}_{i \rightarrow i+1}, \quad i = 0, \dots, N. \quad (33)$$

The advantage of this representation of the model is that the bias condition, Eq. (28), is naturally embedded, and this renders the numerical simulation straightforward and relatively stable. We have used both first-order Euler and fourth-order

Runge-Kutta methods to solve this system Eqs. (26)–(30) and (33), with initial condition

$$E_i(0) = E_{i0}, \quad i = 0, \dots, N, \quad \phi(0) = \sum_{i=0}^N \frac{E_{i0}}{N+1}. \quad (34)$$

The simulations show rapid convergence, so it is not necessary to use higher order or implicit methods.

IV. DEPENDENCE OF TIME-AVERAGED I - V CURVES ON CONTACT CONDUCTIVITY

For larger values of σ , the I - V curves typically exhibit as many stable current branches as there are SL periods. Each branch corresponds to the location of a single static charge accumulation layer in a particular quantum well of the SL. Typically, there is also multistability between adjacent branches. The overall electric field configuration has a high-field domain on the collector side of the SL and low-field domain on the emitter side of the SL. As the contact conductivity is lowered, the static domain configuration loses stability in favor of an oscillatory current. In many respects, the overall behavior is qualitatively similar to that observed for SLs in which the doping level of each period in the SL was lowered from a level that corresponds with intentionally doped structures to undoped structures.^{20,21} However, for very low values of σ , the I - V behavior is not similar to the case of very low doping level and one finds a high-field region next to the emitter contact as discussed below. We have calculated both *ramped* and *time-averaged* I - V curves, and these two possess nearly identical form in regimes where the field profile is time independent. The ramping procedure is as follows: the time step is 1.47 ns and total number of ramping steps from 0 to 4 V and back to 0 V is 8×10^5 , i.e., total ramping time is about 1.2 ms. The up and down sweeps show the presence of hysteresis. The time-averaged I - V curves which we show in the figures below are calculated as follows: at every ramping step described above, the current is averaged over a period of time so long that the time-averaged current value converges, before proceeding to the next voltage. This time is at least 14.7 μ s, much longer than oscillation periods (typically less than 1 μ s).

For the highest value of σ studied here, the I - V curves are composed of regularly spaced, stable branches. Each branch corresponds to a field configuration with a high-field domain near the collector and a low-field domain near the emitter. The two domains are separated by a charge accumulation layer that is mostly confined to two adjacent quantum wells. As the branch number increases by 1, the center of the accumulation layer jumps by one period of the SL, i.e., to a quantum well that is one period closer to the emitter contact. This behavior is clearly shown in Fig. 2(a).

As σ decreases to intermediate values corresponding to Fig. 2(b), the stable current branches become smaller and gaps open up between them. In these gap regions, there is no stable static field configuration and current self-oscillations occur which correspond to the periodic motion of the charge dipole layers across all or part of the SL. This behavior is similar to that reported by Hizanidis *et al.* for a distinct

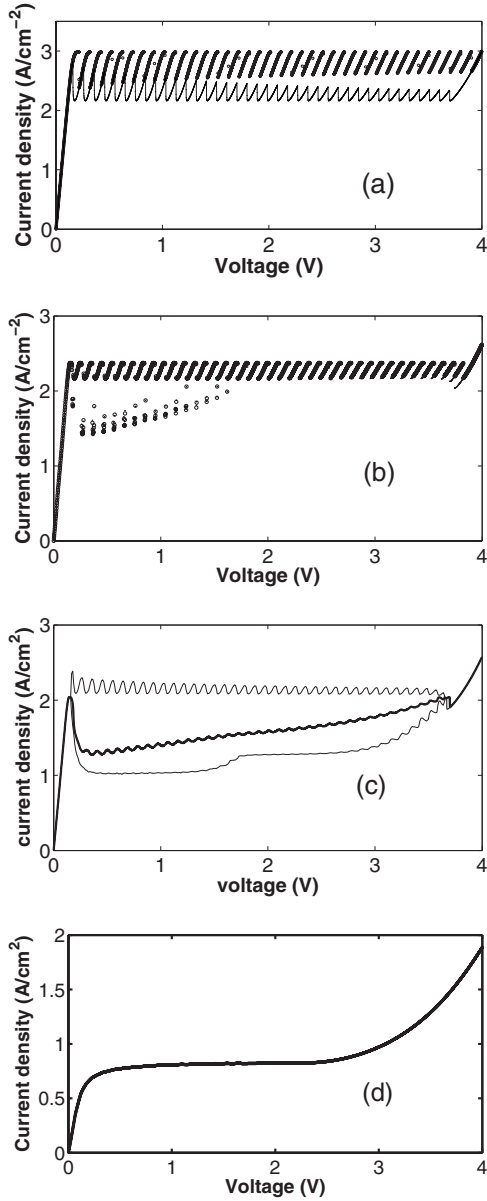


FIG. 2. Time-averaged I - V curves for different σ values: (a) $\sigma = 0.08$ ($\Omega \text{ m}$) $^{-1}$, (b) $\sigma = 0.024$ ($\Omega \text{ m}$) $^{-1}$, (c) $\sigma = 0.016$ ($\Omega \text{ m}$) $^{-1}$, and (d) $\sigma = 0.00168$ ($\Omega \text{ m}$) $^{-1}$. In (c), the thin curves show the envelope of extrema of the time-dependent current.

model of superlattice transport and different device parameters.²⁸ It is likely that the bifurcation diagram of superlattice current behavior versus σ reported in Ref. 28 is also applicable in our system. Finally, it is interesting to note that similar bifurcation behavior is found when the doping level is varied instead of σ , although in the case of intermediate doping levels the current self-oscillations are associated with charge monopoles.²¹

For lower σ values corresponding the Fig. 2(c), the stable branches cease to exist and all the points on the plateau correspond to current self-oscillation, i.e., stable static electric field configurations do not occur for these σ values. The structure of the time-varying electric field profile is that of the dipole layer moving across the entire sample and then

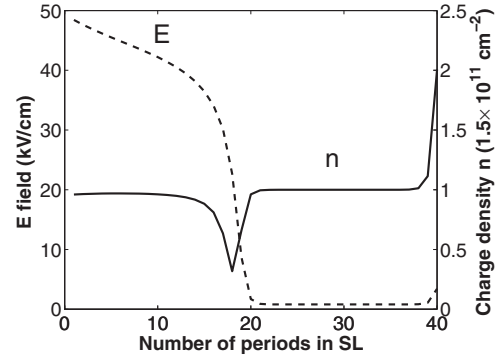


FIG. 3. The spatial profiles of electric field and charge density for applied voltage $V=1$ V and contact conductivity $\sigma = 0.00168$ ($\Omega \text{ m}$) $^{-1}$. A static charge depletion layer separates the high-field region next to the emitter and the low-field domain next to the collector.

recycling and is similar to that found in previous studies.²⁸

Figure 2(d) shows a typical I - V curve for very low σ value such that the contact characteristic sits below the intrinsic J - F characteristic of the SL (cf. Fig. 1). In this case, we find a stable I - V curve without apparent branches or multistability. Remarkably, this corresponds to a stable, static electric field domain configuration in which the low-field domain is adjacent to the collector and a nonconstant high-field region is adjacent to the emitter. These are separated by a static depletion layer that extends over three or more periods, shown in Fig. 3. Because the depletion layer has significantly lower absolute value of charge density than the accumulation layers described above, bistability is not expected or observed in this case. To our knowledge, such a field configuration has not been reported or predicted previously for weakly coupled superlattices though there is evidence for such a field configuration in certain multiple quantum well device structures.⁷ This behavior can be understood by examining the time-independent continuum limit of the discrete rate equation model, Eqs. (20) and (22), which provides a good description provided that the spatial scale of electric field variation is not too rapid. We begin by approximating the field difference in Eq. (21) in terms of the spatial field derivative, i.e., $F_i - F_{i+1} \approx l(\partial F / \partial x)_i$. Substituting this expression into Eq. (21) and solving for n_i allow us to write

$$n_i \approx \frac{\epsilon l}{e} \left(\frac{\partial F}{\partial x} \right)_i + N_D. \quad (35)$$

The current equation, Eq. (23), can be written in time-independent form as

$$\sigma F_0 = J_{i \rightarrow i+1}(n_i, n_{i+1}, F_i), \quad (36)$$

where we have dropped the displacement current and explicitly included the boundary current. Referring back to the expression for well-to-well tunneling current, Eq. (15), we see that, except for fields very close to zero, it is reasonable to include the drift term only so that $J_{i \rightarrow i+1}(n_i, n_{i+1}, F_i) \approx en_i v^f(F_i) / l$.¹⁷ Now, substituting Eq. (35) into Eq. (36) and using the aforementioned drift approximation, we arrive at a

first-order differential equation for the static field profile,

$$\frac{e}{l} \left[\frac{\varepsilon l}{e} \left(\frac{\partial F}{\partial x} \right) + N_D \right] v^f(F) = \sigma F_0. \quad (37)$$

The numerical results are easier to interpret if we write this equation in terms of $\partial F/\partial x$ as follows:

$$\frac{\partial F}{\partial x} = \frac{e N_D}{\varepsilon l} \left(\frac{\sigma F_0}{J_{SL}(F)} - 1 \right), \quad (38)$$

where we have used the drift limit of the SL current-field characteristic under uniform field conditions, $J_{SL}(F) \approx e N_D v^f(F)/l$. Equation (38) provides a good qualitative description of the key features in the field profile of Fig. 3. For instance, the field profile can be calculated by integrating Eq. (38) from $x=0$ (i.e., the injecting contact) into the sample, subject to a boundary condition $F(x=0)=F_0$, where F_0 is ultimately to be determined in terms of the total applied voltage, i.e., $V = \int_0^L F(x) dx$. In the limit of small σ such that $|\sigma F_0| < |J_{SL}(F)|$, we see immediately [from the right-hand side of Eq. (38)] that only regions of depleted charge are possible. Furthermore, the magnitude of depleted charge will be maximal when $|J_{SL}(F)|$ is largest, and this explains the appearance of the predominant depletion layer in the range of wells 17–20. The structure of Eq. (38) also explains why the field profile is not constant in the high-field region between the emitter and the depletion layer: for sufficiently small σ , we have $|\sigma F_0| < |J_{SL}(F)|$ throughout this range of fields and there is a nonzero charge density in this region (corresponding to depletion of electrons) that is approximately uniform—since $J_{SL}(F)$ is approximately constant for these field values, cf. Fig. 1. Furthermore, Eq. (38) gives insight into the shape of the I - V curve at low σ , cf. Fig. 2(d). The plateau occurs because for this range of applied voltages, the boundary field F_0 is almost constant with increasing voltage; the increasing voltage is achieved by the shifting the position of the depletion layer toward the collector.

Equation (38) also allows us to see why the low σ behavior reported here is different from that previously reported for low doping level or, equivalently, for small values of N_D .^{17,21} For σ fixed at a moderately large value, Eq. (38) implies the presence of charge accumulation layers, regardless of the value of N_D . When N_D is small, this leads to stable, static field profiles and I - V curves that are proportional the local SL current-field characteristic.²¹

V. DEPENDENCE OF RELOCATION TYPE ON CONTACT CONDUCTIVITY AND VOLTAGE STEP

We now consider the response of electric field profiles and associated current transients to abrupt steps in applied voltage. We focus on a contact conductivity value $\sigma = 0.064 (\Omega \text{ m})^{-1}$ [which is slightly below the characteristic value defined above, i.e., $\sigma_c \equiv J_M/F_M = 0.07924 (\Omega \text{ m})^{-1}$] and nearby values for which static field domains are stable under time-independent voltage bias. In Fig. 4, we indicate the initial dc voltage by point A and then points B, C, D, and E correspond to the successive final voltages in the following discussion.

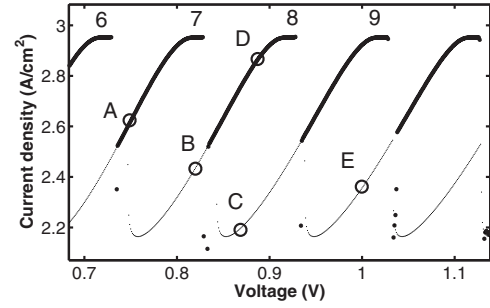


FIG. 4. Initial voltage (A) and successive final voltages (B, C, D, and E) indicated on the I - V curve for $\sigma = 0.064 (\Omega \text{ m})^{-1}$.

The transition from point A (0.75 V) to point B (0.82 V) exhibits the injected dipole process with relatively complex spatiotemporal structure and long relocation time t_r . The corresponding current transient behavior and space-time evolution of the net charge density are shown in Fig. 5. The voltage step causes a current jump which injects electrons into the SL. Prior to the voltage step, there is a small depletion layer at the emitter due to the higher field in the emitter contact; the injected electrons form between the contact and the depletion layer, pushing the depletion layer into the sample. At the same time, the initial accumulation layer jumps back one well, from well 34 to well 33. Then, the small dipole configuration detaches from the emitter and moves into the SL. For the particular conditions shown here,

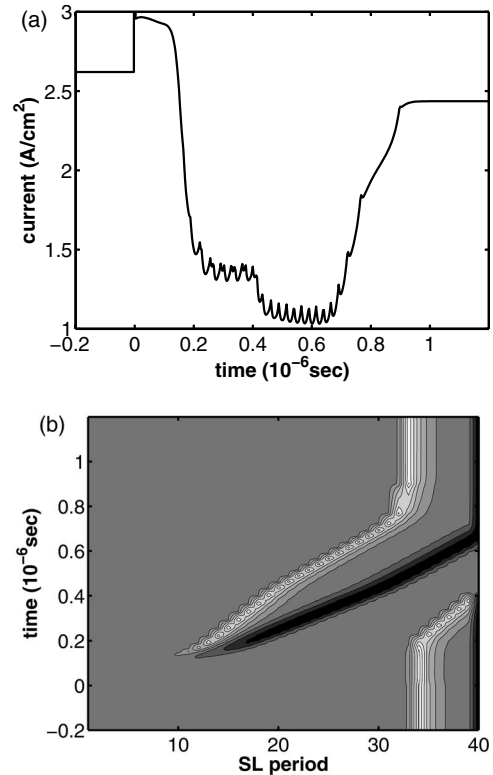


FIG. 5. Injected dipole relocation mechanism for $\sigma = 0.064 (\Omega \text{ m})^{-1}$: (a) transient current response, and (b) space-time portrait of charge density. Voltage switches from 0.75 to 0.82 V (cf. point B in Fig. 4).

it remains small amplitude [so that it is not visible on the gray scale of Fig. 5(b)] and moves at a steady velocity for the first $0.1 \mu\text{s}$ after the voltage step; during this time, the initial accumulation layer remains fixed in well 33 and the current has a large, approximately constant value. After this initial behavior, the dipole layer grows rather abruptly into a moving, fully developed dipole. The initial accumulation layer detaches from well 33 and begins to move toward the collector at the same speed as the accumulation part of the injected dipole. The current drops to a new approximately steady value during this interval—from roughly 0.2 to $0.4 \mu\text{s}$ in Fig. 5(a). The small rapid oscillations in current are due to the motion of the large-amplitude accumulation layers between adjacent wells and these have been discussed previously.^{10,14} These three charge layers move toward the collector and the foremost two layers disappear successively at the collector. Finally, the injected accumulation layer stops at the new position (i.e., well 33) forming the stable field configuration that corresponds to the final voltage. It should be noted that this injected dipole is slightly different than that described in Ref. 14. In that case, a smaller assumed σ value led to the appearance of the fully developed injected dipole beginning at the emitter contact. Additionally, we note that the overall shape of the current transient reflects the prevalence of dipole motion and is similar to that which occurs in the bulk Gunn effect.^{19,27}

As the voltage step size increases, there is a smooth transition to the next scenario, in which the injected dipole layers become smaller and move faster. Thus, the relocation time becomes smaller as shown in Fig. 6 which corresponds to a voltage jump from point A (0.75 V) to point C (0.86965 V) in Fig. 4. In this case, the final accumulation layer is at well 32, two steps closer to the emitter than the initial position. This faster behavior is a direct consequence of the larger voltage step which implies the injection of more electrons. This, in turn, leads to more complete filling of the depletion layer at the emitter resulting in a smaller charge dipole at the emitter. It also can be seen that a small charge layer moves faster than a fully developed one. This can be understood because for a smaller overall charge value in either the accumulation or depletion layer, there is less charge to tunnel through each barrier and the motion is therefore faster.

Further increasing the voltage step, we can see the single monopole shift mechanism shown in Fig. 7, which corresponds to a voltage step from point A (0.75 V) to point D (0.88 V) in Fig. 4. In this scenario, the injected electrons have almost completely filled the depletion layer at the emitter, and the fluctuation is so small that it simply dies out as it begins to move into the SL. The original accumulation layer just moves backward by one period and the whole system reaches a stable state. This process is the simplest and the relocation time is the smallest.

At a large voltage step size that takes the system across two current branches [corresponding to the transition from point A (0.75 V) to E (1.00 V) in Fig. 4], we observe an injected monopole shown in Fig. 8. The large number of injected electrons rapidly fill the depletion layer at the emitter contact and a small accumulation layer is formed at the emitter. This accumulation layer moves rapidly into the SL and comes to rest at the new stable position. The original

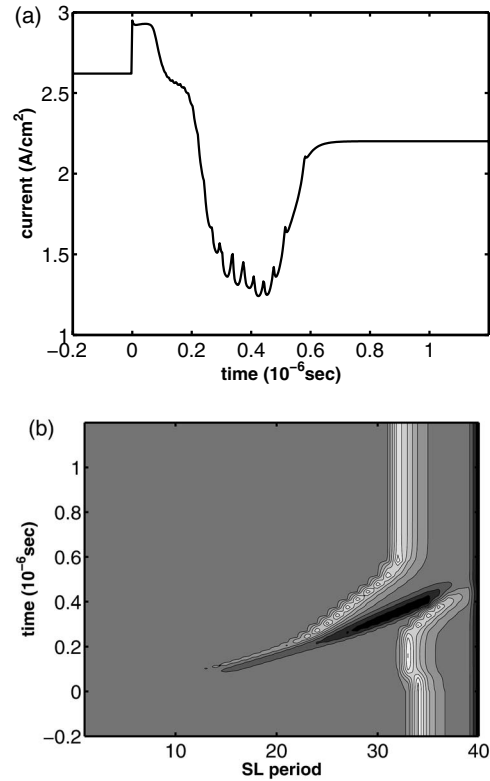


FIG. 6. Shortened injected dipole relocation mechanism for $\sigma = 0.064 (\Omega \text{ m})^{-1}$: (a) transient current response and (b) space-time portrait of charge density. Voltage switches from 0.75 to 0.86965 V (cf. point C in Fig. 4).

accumulation layer simply shrinks and disappears. The relocation time of this process is also relatively short. The initial motion of the small accumulation layer is rapid and it gradually slows as its amplitude increases to the final stable value. At the same time, the current response is strikingly different than that for dipole motion. The overall wave form drops smoothly as the accumulation layer moves into the sample and then rises as the accumulation layer reaches its final location; the intervals of approximately steady current response associated with dipole motion are absent. This behavior is similar to that observed in studies of the bulk Gunn effect in which moving dipole domains were found to give time-periodic current with flat intervals, while moving monopoles were associated with a more sinusoidal current oscillation.^{19,27}

To get a complete picture of the dependence of relocation mechanism and relocation times on contact conductivity, we have computed the relocation time for an entire range of σ and V_{step} values; the results are summarized in Fig. 9. For this figure, the initial voltage is 0.75 V and is in the middle of the seventh branch on the I - V curve. An overall feature of this diagram is that we observe a series of three plateaus with increasing V_{step} . The first plateau, with small V_{step} and independent of σ , corresponds to voltage switching on the same branch in which domain relocation occurs via single monopole shift and is rapid. On the second step, the voltage step crosses one current branch and there is a plateau of long relocation time corresponding to the injected dipole for

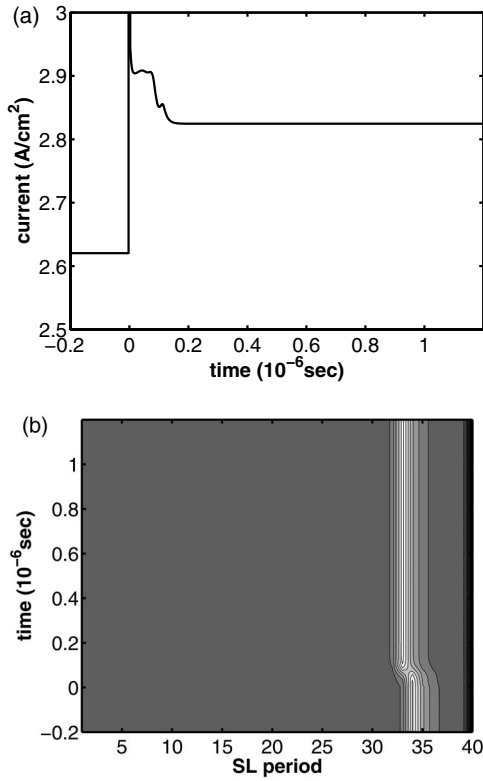


FIG. 7. Single monopole shift $\sigma=0.064$ ($\Omega \text{ m}$)⁻¹: (a) transient current response and (b) space-time portrait of charge density. Voltage switches from 0.75 to 0.88 V (cf. point D in Fig. 4).

smaller values of σ ; however, the relocation time drops sharply for larger values of σ , indicating suppression of the injected dipole for σ values above a characteristic value $\sigma^* \approx 0.072$ ($\Omega \text{ m}$)⁻¹. While this transition is not an abrupt bifurcation point in σ , it does occur over a relatively narrow range of σ values which correspond approximately with the σ value where the contact characteristic no longer intersects the J - F curve in the negative differential conductivity region, cf. Fig. 1 the σ_c value. This suppression occurs because the depletion layer at the emitter becomes small for large σ values so that even a small amount of injected electrons associated with V_{step} can fill the depletion layer before it has a chance to propagate into the SL. The third step mostly consists of shorter relocation time behavior corresponding to the injected monopole mechanism. However, there is a small part of the lower left-hand corner of the third step where injected dipole behavior is observed, and this becomes more prominent for σ values below those shown.

The wall separating the plateau and the first step indicates steady small-amplitude current oscillation behavior that typically occurs at the ends of static current branches. This behavior was first reported in Ref. 13 and corresponds to steady-state oscillation of the accumulation layer between adjacent wells. It is interesting to note that this behavior also ceases for σ values above σ^* , implying that the current branches do not end in small-amplitude oscillations for sufficiently large σ . On the other hand, the ridge between the second and the third steps—which results from metastable behavior during switching and produces a delayed shift—

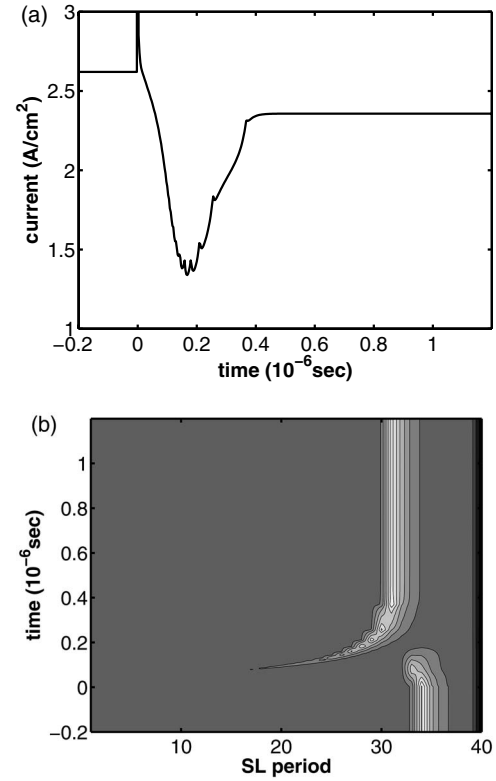


FIG. 8. Injected monopole relocation mechanism for $\sigma=0.064$ ($\Omega \text{ m}$)⁻¹: (a) transient current response and (b) space-time portrait of charge density. Voltage switches from 0.75 to 1.00 V (cf. point E in Fig. 4).

becomes more pronounced for larger σ . This behavior gives rise to nontrivial stochastic switching effects that have been studied experimentally and theoretically.^{9,12} We also note a prevalence of injected monopole behavior for values of σ in excess of the characteristic value σ_c . This behavior is analogous to that found in earlier work on the bulk Gunn effect in which periodically moving dipoles were associated with lower values of σ (i.e., $\sigma < \sigma_c$) while periodically moving charge monopoles were associated with large values of σ (i.e., $\sigma \geq \sigma_c$).¹⁹

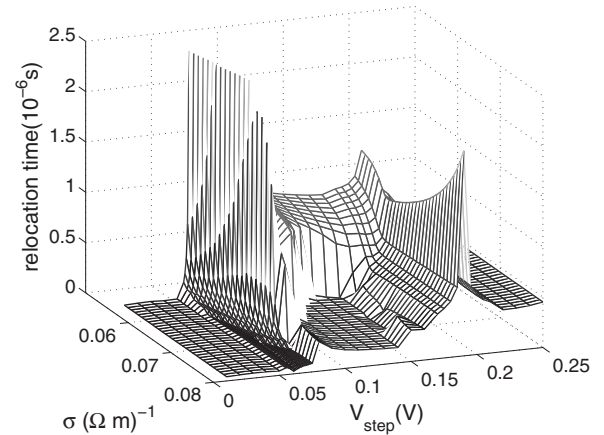


FIG. 9. Dependence of relocation time on voltage step V_{step} and contact conductivity σ . Initial voltage is 0.75 V.

VI. SUMMARY

We have studied how contact conductivity σ , characterizing the boundary condition for the sequential tunneling model, affects the time-averaged I - V characteristics of weakly coupled superlattices and their response to sudden switching of the applied voltage. We find that for relatively large σ values, the I - V curves exhibit static, multistable branches that reflect the presence of a static charge accumulation layer that separates the sample into low- and high-field domains. For intermediate values of σ , the I - V curves reflect the presence of current self-oscillations which are due to the periodic motion of charge dipole layers across portions of the sample. Finally, at very small σ , the I - V curve is a stable curve without branches and reflects an inverted static field-configuration in which the high-field domain is next to the emitter. The overall trend in σ -dependent behavior is seen to result from the role of the contact in setting a limit on the quantity of electrons that enter the superlattice. While there are some similarities between σ dependence and doping density dependence studied previously^{20,21} for large and intermediate conductivity values, the behavior for very small σ is distinct from that occurring for small doping density.

Relocation response to a range of σ values and voltage step values V_{step} is characterized by studying the relocation time t_r and shows that the injected dipole occurs only for a specific range of σ values (within the multistable I - V range) and small V_{step} . Transitional regions are found to occur between different relocation types. A figure of relocation time versus σ and V_{step} , serving as a phase diagram for different relocation types, has been plotted and discussed. The dependence of relocation types on both σ and V_{step} results from the crucial role these two factors play in determining the quantity of electrons that are injected into the superlattice through the emitter contact.

ACKNOWLEDGMENTS

It is a pleasure to acknowledge helpful discussions with Harold Baranger, Luis Bonilla, and Ramon Escobedo.

APPENDIX: RELATIONSHIP BETWEEN CONTACT DOPING DENSITY AND EFFECTIVE CONTACT CONDUCTIVITY

It is useful to relate the experimentally controllable quantity of doping density in the contact region to an equivalent, effective contact conductivity. We have carried this out by treating the emitter as a three-dimensional Fermi gas of electrons in the GaAs contact region, with chemical potential determined by the local (three-dimensional) donor concentration. Inserting this information into the fundamental tunneling current expression, Eq. (4), allows one to derive a microscopically based tunneling current from the emitter into

TABLE II. Relationship between the contact doping density N_{con} and the effective contact conductivity σ .

N_{con} ($\times 10^{18}$ cm $^{-3}$)	1.0	1.1	1.2	1.3	1.4
σ (Ω m) $^{-1}$	0.030	0.036	0.046	0.062	0.106

the first quantum well. The resulting expression can be written as¹⁸

$$J_{0 \rightarrow 1} \approx j_e^{(f)}(F_0) - n_1 w^{(b)}(F_0), \quad (\text{A1})$$

where

$$j_e^{(f)}(F_0) = \sum_{j=1}^n \frac{16k_0^2 k_1^2 \alpha_0^2 (k_0^2 + \alpha_0^2)^{-1} (k_1^2 + \alpha_0^2)^{-1}}{(w + \alpha_0^{-1} + \alpha_1^{-1}) e^{-2\alpha_0 d}} \times \theta \left(\mathcal{E}_j - eF_0 \left(l + \frac{w}{2} \right) \right) \frac{k_B T}{2\pi \hbar} \times \ln \left(1 + \exp \left(\frac{\epsilon_F + eF_0(l + w/2) - \mathcal{E}_j}{k_B T} \right) \right) \quad (\text{A2})$$

and

$$w^{(b)}(F_0) = \frac{8\hbar k_0 k_1^2 \alpha_0^2 (k_0^2 + \alpha_0^2)^{-1} e^{-2\alpha_0 d}}{m^* (w + \alpha_0^{-1} + \alpha_1^{-1}) (k_1^2 + \alpha_0^2)} \theta \left(\mathcal{E}_1 - eF_0 \left(l + \frac{w}{2} \right) \right). \quad (\text{A3})$$

In these expressions, we have used the following definitions:

$$\hbar k_0 = \sqrt{2m^* [\mathcal{E}_j - eF_0(d + w)]}, \quad (\text{A4})$$

$$\hbar k_1 = \sqrt{2m^* \mathcal{E}_j}, \quad (\text{A5})$$

$$\hbar \alpha_0 = \sqrt{2m^* [|e|V_b - \mathcal{E}_j + eF_0(d + w/2)]}, \quad (\text{A6})$$

$$\hbar \alpha_1 = \sqrt{2m^* (|e|V_b - \mathcal{E}_j - eF_0 w/2)}. \quad (\text{A7})$$

Most importantly, ϵ_F denotes the Fermi energy of electrons in the three-dimensional emitter and is expressed in terms of the (three-dimensional) emitter contact doping density N_{con} as

$$\epsilon_F = \frac{\hbar^2}{2m^*} (3\pi^2 N_{con})^{2/3}. \quad (\text{A8})$$

We associate an effective σ value to a particular contact doping density value N_{con} such that the microscopically based contact J - F characteristic of Eq. (A1) and the Ohmic characteristic of Eq. (18) both intersect the J - F curve of the SL at the same point. Results of this calculation are shown in Table II for a range of N_{con} values that are typical for experimental structures. The calculation assumes that all other superlattice parameters are identical with those specified at the end of Sec. II.

- ¹L. Esaki and L. L. Chang, Phys. Rev. Lett. **33**, 495 (1974).
- ²K. K. Choi, B. F. Levine, N. Jarosik, J. Walker, and R. Malik, Phys. Rev. B **38**, 12362 (1988).
- ³J. Kastrup, R. Klann, H. T. Grahn, K. Ploog, L. L. Bonilla, J. Galán, M. Kindelan, M. Moscoso, and R. Merlin, Phys. Rev. B **52**, 13761 (1995).
- ⁴J. Kastrup, R. Hey, K. H. Ploog, H. T. Grahn, L. L. Bonilla, M. Kindelan, M. Moscoso, A. Wacker, and J. Galán, Phys. Rev. B **55**, 2476 (1997).
- ⁵D. Sánchez, M. Moscoso, L. L. Bonilla, G. Platero, and R. Aguado, Phys. Rev. B **60**, 4489 (1999).
- ⁶S. L. Lu, L. Schrottke, S. W. Teitsworth, R. Hey, and H. T. Grahn, Phys. Rev. B **73**, 033311 (2006).
- ⁷H. Schneider, C. Schönbein, R. Rehm, and P. Koidl, Appl. Phys. Lett. **88**, 051114 (2006).
- ⁸K. J. Luo, H. T. Grahn, and K. H. Ploog, Phys. Rev. B **57**, R6838 (1998).
- ⁹M. Rogozia, S. W. Teitsworth, H. T. Grahn, and K. H. Ploog, Phys. Rev. B **64**, 041308(R) (2001).
- ¹⁰M. Rogozia, S. W. Teitsworth, H. T. Grahn, and K. H. Ploog, Phys. Rev. B **65**, 205303 (2002).
- ¹¹M. Rogozia, H. T. Grahn, S. W. Teitsworth, and K. H. Ploog, Physica B **314**, 427 (2002).
- ¹²L. L. Bonilla, O. Sánchez, and J. Soler, Phys. Rev. B **65**, 195308 (2002).
- ¹³L. L. Bonilla, R. Escobedo, and G. Dell'Acqua, Phys. Rev. B **73**, 115341 (2006).
- ¹⁴A. Amann, A. Wacker, L. L. Bonilla, and E. Schöll, Phys. Rev. E **63**, 066207 (2001).
- ¹⁵A. Carpio, L. L. Bonilla, A. Wacker, and E. Schöll, Phys. Rev. E **61**, 4866 (2000).
- ¹⁶G. Platero and R. Aguado, Phys. Rep. **395**, 1 (2004).
- ¹⁷L. L. Bonilla and H. T. Grahn, Rep. Prog. Phys. **68**, 577 (2005).
- ¹⁸L. L. Bonilla, J. Phys.: Condens. Matter **14**, 341 (2002).
- ¹⁹F. J. Higuera and L. L. Bonilla, Physica D **57**, 161 (1992).
- ²⁰M. Patra, G. Schwarz, and E. Schöll, Phys. Rev. B **57**, 1824 (1998).
- ²¹M. Moscoso, L. L. Bonilla, and J. Galan, SIAM J. Appl. Math. **60**, 2029 (2000).
- ²²R. Aguado, G. Platero, M. Moscoso, and L. L. Bonilla, Phys. Rev. B **55**, R16053 (1997).
- ²³M. Jonson, Phys. Rev. B **39**, 5924 (1989).
- ²⁴G. D. Mahan, *Many-Particle Physics*, 2nd ed. (Plenum, New York, 1990), Chaps. 3 and 9.
- ²⁵S. W. Teitsworth and H. Xu (unpublished).
- ²⁶J. Bardeen, Phys. Rev. Lett. **6**, 57 (1961).
- ²⁷H. Kroemer, IEEE Trans. Electron Devices **ED-13**, 27 (1966).
- ²⁸J. Hizanidis, A. Balanov, A. Amann, and E. Schöll, Phys. Rev. Lett. **96**, 244104 (2006).